3-25-2013

Physical Optics Solution for the Scattering of a Partially-coherent Wave from a Statistically Rough Material Surface

Milo W. Hyde IV
Air Force Institute of Technology

Santasri Basu
Air Force Institute of Technology

Mark F. Spencer

Salvatore Cusumano

Steven T. Fiorino
Air Force Institute of Technology

Physical optics solution for the scattering of a partially-coherent wave from a statistically rough material surface

Milo W. Hyde IV,[1,*] Santasri Basu,[1] Mark F. Spencer,[1] Salvatore J. Cusumano,[2] and Steven T. Fiorino[1]

[1]*Air Force Institute of Technology, 2950 Hobson Way, Dayton, OH 45433, USA*
[2]*MZA Associates Corporation, 1360 Technology Court, Suite 200, Dayton, OH 45430, USA*
**milo.hyde@afit.edu*

Abstract: The scattering of a partially-coherent wave from a statistically rough material surface is investigated via derivation of the scattered field cross-spectral density function. Two forms of the cross-spectral density are derived using the physical optics approximation. The first is applicable to smooth-to-moderately rough surfaces and is a complicated expression of source and surface parameters. Physical insight is gleaned from its analytical form and presented in this work. The second form of the cross-spectral density function is applicable to very rough surfaces and is remarkably physical. Its form is discussed at length and closed-form expressions are derived for the angular spectral degree of coherence and spectral density radii. Furthermore, it is found that, under certain circumstances, the cross-spectral density function maintains a Gaussian Schell-model form. This is consistent with published results applicable only in the paraxial regime. Lastly, the closed-form cross-spectral density functions derived here are rigorously validated with scatterometer measurements and full-wave electromagnetic and physical optics simulations. Good agreement is noted between the analytical predictions and the measured and simulated results.

OCIS codes: (030.0030) Coherence and statistical optics; (290.5880) Scattering, rough surfaces; (240.5770) Roughness; (260.2110) Electromagnetic optics.

References and links

1. F. T. Ulaby, R. K. Moore, and A. K. Fung, *Microwave Remote Sensing: Active and Passive* (Artech House, 1986, vol. 2).
2. M.-J. Wang, Z.-S. Wu, and Y.-L. Li, "Investigation on the scattering characteristics of Gaussian beam from two dimensional dielectric rough surfaces based on the Kirchhoff approximation," Prog. Electromagn. Res. B **4**, 223–235 (2008).
3. A. Ishimaru, C. Le, Y. Kuga, L. A. Sengers, and T. K. Chan, "Polarimetric scattering theory for high slope rough surfaces," Prog. Electromagn. Res. **14**, 1–36 (1996).
4. A. Ishimaru, *Wave Propagation and Scattering in Random Media* (IEEE, 1997).
5. G. Guo, S. Li, and Q. Tan, "Statistical properties of laser speckles generated from far rough surfaces," Int. J. Infrared Millimeter Waves **22**, 1177–1191 (2001).
6. V. I. Mandrosov, *Coherent Fields and Images in Remote Sensing* (SPIE, 2004).
7. M. E. Knotts, T. R. Michel, and K. A. O'Donnell, "Angular correlation functions of polarized intensities scattered from a one-dimensionally rough surface," J. Opt. Soc. Am. A **9**, 1822–1831 (1992).
8. S. O. Rice, "Reflection of electromagnetic wave by slightly rough surfaces," Commun. Pure Appl. Math. **4**, 351–378 (1951).
9. A. K. Fung and K. S. Chen, *Microwave Scattering and Emission Models for Users* (Artech House, 2010).

#182849 - $15.00 USD Received 4 Jan 2013; revised 18 Feb 2013; accepted 4 Mar 2013; published 12 Mar 2013

10. R. Axline and A. Fung, "Numerical computation of scattering from a perfectly conducting random surface," IEEE Trans. Antennas Propag. **26**, 482–488 (1978).
11. R. E. Collin, "Full wave theories for rough surface scattering: an updated assessment," Radio Sci. **29**, 1237–1254 (1994).
12. R. Collin, "Scattering of an incident Gaussian beam by a perfectly conducting rough surface," IEEE Trans. Antennas Propag. **42**, 70–74 (1994).
13. E. I. Thorsos, "The validity of the Kirchhoff approximation for rough surface scattering using a Gaussian roughness spectrum," J. Acoust. Soc. Am. **83**, 78–92 (1988).
14. E. Bahar, "Full-wave solutions for the depolarization of the scattered radiation fields by rough surfaces of arbitrary slope," IEEE Trans. Antennas Propag. **29**, 443–454 (1981).
15. T. M. Elfouhaily and C.-A. Guérin, "A critical survey of approximate scattering wave theories from random rough surfaces," Waves Random Media **14**, R1–R40 (2004).
16. K. F. Warnick and W. C. Chew, "Numerical simulation methods for rough surface scattering," Waves Random Media **11**, R1–R30 (2001).
17. A. A. Maradudin, ed., *Light Scattering and Nanoscale Surface Roughness* (Springer, 2007).
18. J. A. Ogilvy, *Theory of Wave Scattering from Random Rough Surfaces* (IOP Publishing, 1991).
19. M. Nieto-Vesperinas, *Scattering and Diffraction in Physical Optics*, 2 ed. (World Scientific, 2006).
20. K. E. Torrance and E. M. Sparrow, "Theory for off-specular reflection from roughened surfaces," J. Opt. Soc. Am. **57**, 1105–1112 (1967).
21. R. G. Priest and S. R. Meier, "Polarimetric microfacet scattering theory with applications to absorptive and reflective surfaces," Opt. Eng. **41**, 988–993 (2002).
22. Y. Sun, "Statistical ray method for deriving reflection models of rough surfaces," J. Opt. Soc. Am. A **24**, 724–744 (2007).
23. P. Beckmann and A. Spizzichino, *The Scattering of Electromagnetic Waves from Rough Surfaces* (Pergamon, 1963).
24. X. D. He, K. E. Torrance, F. X. Sillion, and D. P. Greenberg, "A comprehensive physical model for light reflection," SIGGRAPH Computer Graphics **25**, 175–186 (1991).
25. J. Dainty, "Some statistical properties of random speckle patterns in coherent and partially coherent illumination," Opt. Acta **17**, 761–772 (1970).
26. J. Goodman, "Statistical properties of laser speckle patterns," in "Laser Speckle and Related Phenomena," vol. 9 of *Topics in Applied Physics*, J. C. Dainty, ed. (Springer-Verlag, 1975, pp. 9–75).
27. G. Parry, "Speckle patterns in partially coherent light," in "Laser Speckle and Related Phenomena," vol. 9 of *Topics in Applied Physics*, J. C. Dainty, ed. (Springer-Verlag, 1975, pp. 77–121).
28. H. Fujii and T. Asakura, "A contrast variation of image speckle intensity under illumination of partially coherent light," Opt. Commun. **12**, 32–38 (1974).
29. H. Fujii and T. Asakura, "Statistical properties of image speckle patterns in partially coherent light," Nouv. Rev. Opt. **6**, 5–14 (1975).
30. H. Pedersen, "The roughness dependence of partially developed, monochromatic speckle patterns," Opt. Commun. **12**, 156–159 (1974).
31. T. Yoshimura, K. Kato, and K. Nakagawa, "Surface-roughness dependence of the intensity correlation function under speckle-pattern illumination," J. Opt. Soc. Am. A **7**, 2254–2259 (1990).
32. J. W. Goodman, *Speckle Phenomena in Optics: Theory and Applications* (Ben Roberts & Company, 2007).
33. L. Mandel and E. Wolf, *Optical Coherence and Quantum Optics* (Cambridge University, 1995).
34. E. Wolf, "Unified theory of coherence and polarization of random electromagnetic beams," Phys. Lett. A **312**, 263–267 (2003).
35. E. Wolf, *Introduction to the Theory of Coherence and Polarization of Light* (Cambridge University, 2007).
36. G. Gbur and T. Visser, "The structure of partially coherent fields," Progress in Optics **55**, 285–341 (2010).
37. O. Korotkova, M. Salem, and E. Wolf, "The far-zone behavior of the degree of polarization of electromagnetic beams propagating through atmospheric turbulence," Opt. Commun. **233**, 225–230 (2004).
38. O. Korotkova, T. Visser, and E. Wolf, "Polarization properties of stochastic electromagnetic beams," Opt. Commun. **281**, 515–520 (2008).
39. T. Leskova, A. Maradudin, and J. Muñoz-Lopez, "The design of one-dimensional randomly rough surfaces that act as Collett-Wolf sources," Opt. Commun. **242**, 123–133 (2004).
40. J. Li, Y. Chen, S. Xu, Y. Wang, M. Zhou, Q. Zhao, Y. Xin, and F. Chen, "Condition for invariant spectral degree of coherence of an electromagnetic plane wave on scattering," Opt. Commun. **284**, 724–728 (2011).
41. T. Wang and D. Zhao, "Stokes parameters of an electromagnetic light wave on scattering," Opt. Commun. **285**, 893–895 (2012).
42. T. Shirai and T. Asakura, "Multiple light scattering from spatially random media under the second-order Born approximation," Opt. Commun. **123**, 234–249 (1996).
43. G. Gbur and E. Wolf, "Determination of density correlation functions from scattering of polychromatic light," Opt. Commun. **168**, 39–45 (1999).
44. F. Gori, C. Palma, and M. Santarsiero, "A scattering experiment with partially coherent light," Opt. Commun. **74**,

#182849 - $15.00 USD Received 4 Jan 2013; revised 18 Feb 2013; accepted 4 Mar 2013; published 12 Mar 2013

353–356 (1990).
45. E. Wolf, J. T. Foley, and F. Gori, "Frequency shifts of spectral lines produced by scattering from spatially random media," J. Opt. Soc. Am. A **6**, 1142–1149 (1989).
46. B. G. Hoover and V. L. Gamiz, "Coherence solution for bidirectional reflectance distributions of surfaces with wavelength-scale statistics," J. Opt. Soc. Am. A **23**, 314–328 (2006).
47. L. C. Andrews and R. L. Phillips, *Laser Beam Propagation through Random Media*, 2 ed. (SPIE, 2005).
48. O. Korotkova, *Partially Coherent Beam Propagation in Turbulent Atmosphere with Applications* (VDM Verlag Dr. Müller, 2009).
49. R. S. Hansen, H. T. Yura, and S. G. Hanson, "First-order speckle statistics: an analytic analysis using ABCD matrices," J. Opt. Soc. Am. A **14**, 3093–3098 (1997).
50. H. Yura and S. Hanson, "Variance of intensity for Gaussian statistics and partially developed speckle in complex ABCD optical systems," Opt. Commun. **228**, 263–270 (2003).
51. S. Sahin, Z. Tong, and O. Korotkova, "Sensing of semi-rough targets embedded in atmospheric turbulence by means of stochastic electromagnetic beams," Opt. Commun. **283**, 4512–4518 (2010).
52. J. Huttunen, A. T. Friberg, and J. Turunen, "Scattering of partially coherent electromagnetic fields by microstructured media," Phys. Rev. E **52**, 3081–3092 (1995).
53. M. W. Hyde, S. Basu, S. J. Cusumano, and M. F. Spencer, "Scalar wave solution for the scattering of a partially coherent beam from a statistically rough metallic surface," Proc. SPIE **8550** (2012).
54. T. Hansen and A. Yaghjian, *Plane-Wave Theory of Time-Domain Fields: Near-Field Scanning Applications* (IEEE, 1999).
55. S. Ramo, J. Whinnery, and T. Van Duzer, *Fields and Waves in Communication Electronics*, 3 ed. (John Wiley & Sons, 1994).
56. C. A. Mack, "Analytic form for the power spectral density in one, two, and three dimensions," J. Micro/Nanolithogr. MEMS MOEMS **10**, 040501 (2011).
57. S. Basu, S. J. Cusumano, M. W. Hyde, M. A. Marciniak, and S. T. Fiorino, "Validity of using Gaussian Schell model for extended beacon studies," Proc. SPIE **8380** (2012).
58. Under quasi-monochromatic conditions ($\Delta\omega \ll \bar{\omega}$), $S(\boldsymbol{\rho},\omega) \approx \Gamma(\boldsymbol{\rho},\boldsymbol{\rho},0)\,\delta(\omega-\bar{\omega})$ and $\mu(\boldsymbol{\rho}_1,\boldsymbol{\rho}_2,\omega) \approx \gamma(\boldsymbol{\rho}_1,\boldsymbol{\rho}_2,\tau)\exp(\mathrm{j}\bar{\omega}\tau)$. Here, Γ is the mutual coherence function and γ is the complex degree of coherence [59].
59. A. T. Friberg and E. Wolf, "Relationships between the complex degrees of coherence in the space-time and in the space-frequency domains," Opt. Lett. **20**, 623–625 (1995).
60. B. Balling, "A comparative study of the bidirectional reflectance distribution function of several surfaces as a mid-wave infrared diffuse reflectance standard," Master's thesis, Graduate School of Engineering and Management, Air Force Institute of Technology (AETC), Wright-Patterson AFB OH (2009). http://oai.dtic.mil/oai/oai?verb=getRecord&metadataPrefix=html&identifier=ADA495933.
61. LabSphere, Inc., "A guide to reflectance coatings and materials" (LabSphere, Inc., 2012). http://www.labsphere.com/uploads/technical-guides/a-guide-to-reflectance-materials-and-coatings.pdf.
62. KLA-Tencor Corporation, "Alpha-Step IQ Surface Profiler" (KLA-Tencor Corporation, 2012). http://www.kla-tencor.com/surface-profiling/alpha-step-iq.html.
63. R. Harrington, *Field Computation by Moment Methods* (IEEE, 1993).
64. A. F. Peterson, S. L. Ray, and R. Mittra, *Computational Methods for Electromagnetics* (IEEE, 1998).
65. RefractiveIndex.INFO, "RefractiveIndex.INFO Refractive index database" (RefractiveIndex.INFO, 2012). http://refractiveindex.info.
66. H. T. Yura and S. G. Hanson, "Digital simulation of an arbitrary stationary stochastic process by spectral representation," J. Opt. Soc. Am. A **28**, 675–685 (2011).
67. X. Xiao and D. Voelz, "Wave optics simulation approach for partial spatially coherent beams," Opt. Express **14**, 6986–6992 (2006).

1. Introduction

Rough surface scattering has been an active area of research for a half century. The published research on the subject can generally be divided into two main groups. The first deals with rough surface scattering research performed by the RF/microwave community for synthetic aperture radar and remote sensing applications. Predominately concerned with fully-coherent, monochromatic plane-wave scattering from rough surfaces (with some exceptions), the common approaches employed by the RF/microwave community to the rough surface scattering problem are physical optics (PO) [1–7], perturbation [4, 8], and computational/full-wave [9–14] methods. The interested reader is referred to Elfouhaily and Guérin [15], Warnick and Chew [16], Maradudin [17], Ogilvy [18], and Nieto-Vesperinas [19] for excellent summaries of these techniques.

#182849 - $15.00 USD Received 4 Jan 2013; revised 18 Feb 2013; accepted 4 Mar 2013; published 12 Mar 2013

The second of the two main groups deals with rough surface scattering research performed by the optics community. Initially, this work mainly dealt with how incoherent light interacted with surfaces, modeled via the bidirectional reflectance distribution function (BRDF), for applications in passive visible/near-IR remote sensing and computer graphics [20–24]. More recently, with the proliferation of laser-based systems (LIDAR/LADAR and directed energy), the interaction of coherent laser light with rough surfaces, in particular the statistical behaviors of the resulting speckle patterns, gained considerable interest in such fields as metrology and remote sensing. Some of the early notable research in this area was performed by Dainty [25], Goodman [26], Parry [27], Fujii and Asakura [28,29], Pedersen [30], and Yoshimura *et al.* [31].

Since the presence of speckle is typically detrimental in applications involving coherent light, techniques for suppressing speckle naturally followed. While there are many such techniques [32], due predominately to the work of Wolf [33–35], the use of partially-coherent light, instead of laser light, in active illumination systems is becoming tremendously popular for speckle suppression. In particular, much literature is dedicated to the properties of partially-coherent light whose cross-spectral density (CSD) function possesses a Gaussian Schell-model (GSM) form [33, 35–39]. In regards to the scattering of partially-coherent light, most of the current literature deals with scattering from low-contrast scatterers, i.e., for scatterers in which the Born approximation is valid [33, 35, 36, 40–45]. Far less work has been performed analyzing the scattering of partially-coherent light from rough metallic surfaces. Of the work that has been published, the following approaches are common: the phase-screen model [32, 46–48], ABCD matrices [47–51], and the coherent-mode representation [52].

The purpose of this rough surface scattering work is to extend the traditional, fully-coherent approaches to cases involving partially-coherent illumination. Previous work by the authors derived analytical forms for the scattering of a partially-coherent beam from a statistically rough perfectly-reflecting surface using the PO approximation [53]. In this work, the previously derived scattering solutions are generalized to material surfaces and rigorously verified via experiment and simulation.

Two forms of the scattered field CSD function are derived and discussed. The first, applicable to surfaces of smooth-to-moderate roughness, is expressed in terms of an infinite series. While its behavior depends in a complex way on source and surface parameters, its analytical form is physically intuitive. The second form of the scattered field CSD function is applicable to very rough surfaces. This form of the CSD function is incredibly physical and, under certain circumstances, maintains a GSM form, which is in agreement with the literature cited above valid in the paraxial regime. As such, closed-form expressions are derived for the angular spectral degree of coherence (SDoC) and spectral density (SD) radii. These expressions are, in general, complicated functions of both the source and surface parameters. It is demonstrated that for many scenarios of interest, the SDoC radius can be safely approximated as a function of just the source parameters and the SD radius can be simplified to a function of just the surface parameters.

To verify the theoretical analysis, experimental and Monte Carlo simulation results using a full-wave electromagnetic technique (all the physics of the wave/surface interaction are included) and one based on the PO approximation are presented and compared to the predictions of the analytical models. This paper is concluded with a summary of the work and contributions presented.

2. Methodology

The scattering geometry utilized in this analysis is shown in Fig. 1. The surface height is described by the function $h(x)$ with mean, standard deviation, and correlation length equal to 0, σ_h, and ℓ_h, respectively. The surface (of length $2L$) is illuminated by a partially-coherent beam

#182849 - $15.00 USD Received 4 Jan 2013; revised 18 Feb 2013; accepted 4 Mar 2013; published 12 Mar 2013

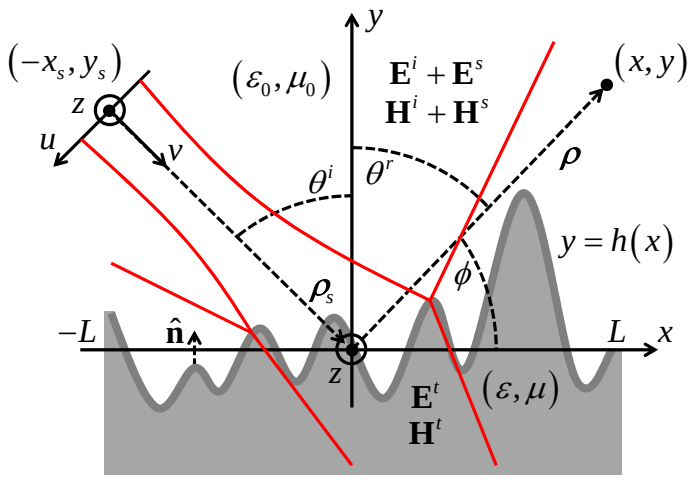

Fig. 1. Scattering geometry of a one-dimensional (the surface and source excitation are invariant in the z direction) rough surface of length $2L$. The medium below the rough interface is electrically defined by the permittivity ε and permeability μ; the medium above the rough interface is vacuum (ε_0, μ_0). The rough surface height is described by the function $h(x)$; the mean, standard deviation, and correlation length of the surface are 0, σ_h, and ℓ_h, respectively. The point $(-x_s, y_s)$ denotes the location of the source plane origin. The observation vector $\boldsymbol{\rho} = \hat{\mathbf{x}}x + \hat{\mathbf{y}}y$ points from the rough surface origin to the observation point. The vector $\boldsymbol{\rho}_s = \hat{\mathbf{x}}x_s - \hat{\mathbf{y}}y_s$ points from the source plane origin to the rough surface origin.

(parameters w_s and ℓ_s defined below) emanating from the source plane specified by the coordinates (u, v, z). Its origin, relative to the rough surface coordinate system, is located at the point $(-x_s, y_s)$. The observation vector $\boldsymbol{\rho} = \hat{\mathbf{x}}x + \hat{\mathbf{y}}y$ points from the rough surface origin to the observation point. The medium below the rough interface is electrically described by the permittivity ε and permeability μ; the medium above the rough interface is vacuum (ε_0, μ_0).

A GSM form for the incident field CSD is used to model the partially-coherent illumination, viz.,

$$W^i(u_1, u_2) = \left\langle E^i(u_1) E^{i*}(u_2) \right\rangle = E_0^2 \exp\left(-\frac{u_1^2 + u_2^2}{4w_s^2}\right) \exp\left[-\frac{(u_1 - u_2)^2}{2\ell_s^2}\right], \tag{1}$$

where w_s and ℓ_s are the source radius and source coherence radius, respectively and the functional dependence of W^i, E_0, w_s, and ℓ_s on the radian frequency ω is omitted for brevity [33,35]. Both s-pol and p-pol scattering solutions are derived below. Note that the rough surface and the source excitation are invariant in the z direction resulting in a two-dimensional scattering problem. As mentioned by Johnson [17], light scattered from one-dimensional surfaces demonstrates the same physical behaviors as light scattered from two-dimensional surfaces. The mechanisms which are not captured in two-dimensional scattering problems are cross-polarized scattering and out-of-plane scattering [17]. In this way, the expressions derived in this paper are equivalent to scalar-wave scattering solutions.

2.1. PO expression for the scattered field

For the sake of brevity, the analysis to follow focuses on perpendicular polarization. The solution for parallel polarization is provided at the end of the section. For perpendicular polarization,

#182849 - $15.00 USD Received 4 Jan 2013; revised 18 Feb 2013; accepted 4 Mar 2013; published 12 Mar 2013

the incident field in the source plane takes the form

$$\mathbf{E}^i = \hat{\mathbf{z}} E_z^i(u). \tag{2}$$

Utilizing the plane-wave spectrum representation of electromagnetic fields [54], the incident electric and magnetic fields become

$$\begin{aligned} \mathbf{E}^i &= \frac{1}{2\pi}\int_{-\infty}^{\infty} \mathbf{T}_e^i\left(k_u^i\right)\exp\left(-\mathrm{j}\mathbf{k}^i\cdot\boldsymbol{\rho}_s\right)\exp\left(-\mathrm{j}\mathbf{k}^i\cdot\boldsymbol{\rho}\right)\mathrm{d}k_u^i \quad v>0 \\ \mathbf{H}^i &= \frac{1}{2\pi}\int_{-\infty}^{\infty} \frac{\mathbf{k}^i\times\mathbf{T}_e^i\left(k_u^i\right)}{\omega\mu_0}\exp\left(-\mathrm{j}\mathbf{k}^i\cdot\boldsymbol{\rho}_s\right)\exp\left(-\mathrm{j}\mathbf{k}^i\cdot\boldsymbol{\rho}\right)\mathrm{d}k_u^i \quad v>0 \end{aligned}, \tag{3}$$

where $\boldsymbol{\rho}_s$ is a vector that points from the source plane origin to the rough surface origin, $\mathbf{k}^i = \hat{\mathbf{u}}k_u^i + \hat{\mathbf{v}}k_v^i$, and

$$\mathbf{T}_e^i\left(k_u^i\right) = \hat{\mathbf{z}}\int_{-\infty}^{\infty} E_z^i(u)\exp\left(\mathrm{j}k_u^i u\right)\mathrm{d}u. \tag{4}$$

Note that $\left|\mathbf{k}^i\right| = k_0 = 2\pi/\lambda$, thus $k_v^i = \sqrt{k_0^2 - \left(k_u^i\right)^2}$.

The scattered field in the far zone can be found by utilizing the transverse components of the far-field vector potentials $\mathbf{N}$ and $\mathbf{L}$ [55] and the equivalent electric $\mathbf{J}$ and magnetic $\mathbf{M}$ currents induced on the rough surface by the incident field, namely,

$$\begin{aligned} \mathbf{E}^s &\approx \sqrt{\frac{\mathrm{j}k_0}{8\pi}}\frac{\exp\left(-\mathrm{j}k_0\rho\right)}{\sqrt{\rho}}\left[-\sqrt{\frac{\mu_0}{\varepsilon_0}}\mathbf{N}_t + \mathbf{L}_t\right] \\ \mathbf{N}_t &= \left(\hat{\phi}\hat{\phi} + \hat{\mathbf{z}}\hat{\mathbf{z}}\right)\cdot\int_C \mathbf{J}\left(\boldsymbol{\rho}'\right)\exp\left(\mathrm{j}k_0\hat{\boldsymbol{\rho}}\cdot\boldsymbol{\rho}'\right)\mathrm{d}c \\ \mathbf{L}_t &= \left(\hat{\phi}\hat{\phi} + \hat{\mathbf{z}}\hat{\mathbf{z}}\right)\cdot\int_C \mathbf{M}\left(\boldsymbol{\rho}'\right)\exp\left(\mathrm{j}k_0\hat{\boldsymbol{\rho}}\cdot\boldsymbol{\rho}'\right)\mathrm{d}c \end{aligned}, \tag{5}$$

where $\boldsymbol{\rho}' = \hat{\mathbf{x}}x' + \hat{\mathbf{y}}h(x')$. Note that the integral is over the parameterized surface contour C with $\mathrm{d}c$ equal to the arc length, i.e., $\mathrm{d}c = \mathrm{d}x'\sqrt{1+\left[h'(x')\right]^2}$.

Using the PO approximation, the equivalent currents induced by the incident field on the material surface are

$$\begin{aligned} \mathbf{J} &\approx \left(1-r_\perp\right)\hat{\mathbf{n}}\times\mathbf{H}^i\big|_{\substack{x=x' \\ y=h(x')}} \\ \mathbf{M} &\approx \left(1+r_\perp\right)\mathbf{E}^i\times\hat{\mathbf{n}}\big|_{\substack{x=x' \\ y=h(x')}} \end{aligned}. \tag{6}$$

Here, $\hat{\mathbf{n}}$ is the unit outward normal to the surface given by

$$\hat{\mathbf{n}} = \frac{\hat{\mathbf{y}} - \hat{\mathbf{x}}h'(x)}{\sqrt{1+\left[h'(x)\right]^2}} = \frac{\hat{\mathbf{y}} - \hat{\mathbf{x}}h_x}{\sqrt{1+h_x^2}} \tag{7}$$

and $r_\perp$ is the s-pol Fresnel complex amplitude reflection coefficient. Substitution of Eqs. (6) and (7) into Eq. (5) and subsequent simplification yields the following expression for E_z^s:

$$E_z^s = \frac{\exp\left(-\mathrm{j}k_0\rho + \mathrm{j}\frac{\pi}{4}\right)}{2\pi\sqrt{8\pi k_0\rho}}\int_{-\infty}^{\infty} T_{ez}^i\left(k_u^i\right)e^{-\mathrm{j}\mathbf{k}^i\cdot\boldsymbol{\rho}_s}\int_{-L}^{L}\mathscr{H}_\perp\left(x',k_u^i\right)e^{\mathrm{j}\boldsymbol{\nu}\cdot\boldsymbol{\rho}'}\mathrm{d}x'\mathrm{d}k_u^i, \tag{8}$$

#182849 - $15.00 USD Received 4 Jan 2013; revised 18 Feb 2013; accepted 4 Mar 2013; published 12 Mar 2013

where $\boldsymbol{\nu} = k_0\hat{\boldsymbol{\rho}} - \mathbf{k}^i$ and

$$\mathscr{H}_\perp\left(x', k_u^i\right) = \left(1 - r'_\perp\right)\left(k_v^i\hat{\mathbf{u}} - k_u^i\hat{\mathbf{v}}\right)\cdot\left(\hat{\mathbf{x}} + \hat{\mathbf{y}}h_{x'}\right) + k_0\left(1 + r'_\perp\right)\hat{\boldsymbol{\rho}}\cdot\left(\hat{\mathbf{y}} - \hat{\mathbf{x}}h_{x'}\right). \tag{9}$$

Note that $r_\perp$ is primed because it is a function of surface coordinates $(x', h(x'))$.

No analytical solution has yet been found for the integral over the rough surface coordinate x' in Eq. (8) because of $\mathscr{H}_\perp$, which is a complicated function of $h(x')$ and its derivative $h_{x'}$ [1]. This integral is typically evaluated using the stationary-phase approximation in which $h_{x'} \approx -\nu_x/\nu_y$ [1,19]. This approximation physically dictates that reflection from the rough surface is locally specular, i.e., local diffraction effects are excluded [1, 17–19, 23]. Applying this approximation to Eq. (8) and rearranging the integrals results in

$$E_z^s = \frac{\exp\left(-\mathrm{j}k_0\rho + \mathrm{j}\frac{\pi}{4}\right)}{2\pi\sqrt{8\pi k_0\rho}}\int_{-L}^{L}\int_{-\infty}^{\infty}\mathscr{H}_\perp\left(k_u^i\right)T_{ez}^i\left(k_u^i\right)e^{-\mathrm{j}\mathbf{k}^i\cdot\boldsymbol{\rho}_s}e^{\mathrm{j}\boldsymbol{\nu}\cdot\boldsymbol{\rho}'}\mathrm{d}x'\mathrm{d}k_u^i. \tag{10}$$

This expression represents the s-pol scattered electric field given one random incident field and one random surface realization. The only assumptions that have been made thus far are that observation is in the far field, the rough surface is such that the PO approximation for the currents holds, and shadowing/masking and multiple scattering can be safely neglected [18,19].

2.2. *Scattered field cross-spectral density function*

Applying the definition of the autocorrelation of a random process to Eq. (10) yields

$$\begin{aligned} W^s(\boldsymbol{\rho}_1, \boldsymbol{\rho}_2) &= \left\langle E_z^s(\boldsymbol{\rho}_1)E_z^{s*}(\boldsymbol{\rho}_2)\right\rangle \\ &= \frac{e^{\mathrm{j}k_0(\rho_2-\rho_1)}}{32\pi^3k_0\sqrt{\rho_1\rho_2}}\int_{-L}^{L}\int_{-L}^{L}\int_{-\infty}^{\infty}\int_{-\infty}^{\infty}\mathscr{H}_{\perp 1}\mathscr{H}_{\perp 2}^*e^{\mathrm{j}\left(\mathbf{k}_2^i-\mathbf{k}_1^i\right)\cdot\boldsymbol{\rho}_s}, \\ &\quad \left\langle T_{ez1}^iT_{ez2}^{i*}\right\rangle\left\langle e^{\mathrm{j}\boldsymbol{\nu}_1\cdot\boldsymbol{\rho}'_1}e^{-\mathrm{j}\boldsymbol{\nu}_2\cdot\boldsymbol{\rho}'_2}\right\rangle\mathrm{d}k_{u1}^i\mathrm{d}k_{u2}^i\mathrm{d}x'_1\mathrm{d}x'_2 \end{aligned} \tag{11}$$

where the subscripts 1 and 2 imply that the associated expression is a function of $x'_1, \boldsymbol{\rho}_1, k_{u1}^i$ or $x'_2, \boldsymbol{\rho}_2, k_{u2}^i$ (whichever is applicable), respectively, and the expectations are computed over the ensembles of rough surface and incident field realizations. In arriving at the above expression, it has been assumed that the incident field plane-wave spectrum is statistically independent of the rough surface; this assumption is physically intuitive. Note that the autocorrelation of the incident field plane-wave spectrum is equivalent to the Fourier transform of the CSD function given in Eq. (1). The second autocorrelation expression in Eq. (11), after some simple manipulation, is equivalent to the joint characteristic function of the random variables $h(x'_1)$ and $h(x'_2)$ [23]. The incident field term and the rough surface term are represented as $\Phi\left(k_{u1}^i, k_{u2}^i\right)$ and $\chi\left(k_{u1}^i, k_{u2}^i; x'_1, x'_2\right)$ in the analysis to follow.

The integrals over the incident field plane-wave spectrum can be approximated using the method of stationary phase [33]. Using the method of stationary phase to evaluate the plane-wave spectrum integrals has two implications. The first is that $k_v^i \gg k_u^i$ and is therefore approximated as $k_v^i \approx k_0 - \left(k_u^i\right)^2/(2k_0)$ for all "phase" terms (i.e., $\exp[\mathrm{j}(\cdots)]$) and as $k_v^i \approx k_0$ for all amplitude terms. This physically implies that the incident field is highly directional being predominately directed along the v direction in Fig. 1. The second implication is that the distance from the rough surface to the source plane ρ_s must be much greater than L—this is generally the case. To provide some idea of how much greater ρ_s must be than L, $\rho_s = 10L$, $\rho_s = 20L$, and $\rho_s = 50L$ are approximately 95%, 97.5%, and 99% accurate, respectively. Note that these two implications mean that the $k_u^i\hat{\mathbf{v}}$ term in $\mathscr{H}_\perp$, see Eq. (9), diminishes at the rate of $1/\rho_s$

#182849 - $15.00 USD Received 4 Jan 2013; revised 18 Feb 2013; accepted 4 Mar 2013; published 12 Mar 2013

and therefore can be neglected. Recall that this term corresponded to the $\hat{\mathbf{v}}$ component of the incident magnetic field implying that the field incident on the rough surface is transverse electromagnetic (in particular, TEM^v) when the method of stationary phase is utilized. Applying the method of stationary phase and substituting in $\Phi\left(k_{u1}^i, k_{u2}^i\right)$ produces

$$\begin{aligned} W^s\left(\boldsymbol{\rho}_1, \boldsymbol{\rho}_2\right) = & \frac{E_0^2 k_0^2 e^{\mathrm{j}k_0(\rho_2-\rho_1)}\mathscr{S}^{\perp}}{16\pi\rho_s\sqrt{\rho_1\rho_2\left(a^2-b^2\right)}} \int_{-L}^{L}\int_{-L}^{L} \exp\left[-\tilde{a}\frac{k_0^2(\hat{\mathbf{x}}\cdot\hat{\mathbf{u}})^2}{\rho_s^2}\left(x_1'^2+x_2'^2\right)\right] \\ & \exp\left[2\tilde{b}\frac{k_0^2(\hat{\mathbf{x}}\cdot\hat{\mathbf{u}})^2}{\rho_s^2}x_1'x_2'\right]\exp\left[\mathrm{j}\frac{k_0(\hat{\mathbf{x}}\cdot\hat{\mathbf{u}})^2}{2\rho_s}\left(x_2'^2-x_1'^2\right)\right]e^{\mathrm{j}k_0(\hat{\mathbf{x}}\cdot\hat{\mathbf{v}})\left(x_1'-x_2'\right)}, \\ & \chi\left(\frac{k_0\left(\hat{\mathbf{x}}\cdot\hat{\mathbf{u}}\right)x_1'}{\rho_s}, \frac{k_0\left(\hat{\mathbf{x}}\cdot\hat{\mathbf{u}}\right)x_2'}{\rho_s}; x_1', x_2'\right)e^{\mathrm{j}k_0\left[(\hat{\mathbf{x}}\cdot\hat{\boldsymbol{\rho}}_1)x_1'-(\hat{\mathbf{x}}\cdot\hat{\boldsymbol{\rho}}_2)x_2'\right]}\mathrm{d}x_1'\mathrm{d}x_2' \end{aligned} \tag{12}$$

where the symbols used above are defined in the appendix.

To simplify Eq. (12) further, a form for the rough surface characteristic function χ must be chosen. A very common choice for the statistical distribution of the rough surface is to assume that the surface heights are Gaussian distributed and Gaussian correlated, i.e.,

$$\begin{aligned} p_{H_1,H_2}\left(h_1,h_2\right) &= \frac{1}{2\pi\sigma_h^2\sqrt{1-\Gamma^2}}\exp\left[-\frac{h_1^2-2\Gamma h_1h_2+h_2^2}{2\sigma_h^2\left(1-\Gamma^2\right)}\right] \\ \Gamma\left(x_1'-x_2'\right) &= \exp\left[-\frac{\left(x_1'-x_2'\right)^2}{\ell_h^2}\right] \end{aligned}. \tag{13}$$

Historically, Gaussian-Gaussian (G-G) models for rough surfaces were chosen for analytical convenience [32]. Recent profilometer measurements of sandblasted metallic surfaces showed that the stretched exponential-stretched exponential (SE-SE) model [56] more accurately represented surfaces roughened by random industrial processes [57]. Unfortunately, no general analytical form for the SE joint characteristic function exists. Although the results in [57] indicated that SE-SE models were superior, G-G models were fairly good approximations for the surfaces that were measured. Note that, in addition to G-G and SE-SE, numerous other surface models can be found throughout the literature. Fourier transforming the above joint probability density function yields the desired characteristic function:

$$\chi\left(k_{u1}^i, k_{u2}^i; x_1', x_2'\right) = \exp\left[-\frac{\sigma_h^2}{2}\left(\nu_{y1}^2+\nu_{y2}^2\right)\right]\exp\left\{\sigma_h^2\nu_{y1}\nu_{y2}\exp\left[-\frac{\left(x_1'-x_2'\right)^2}{\ell_h^2}\right]\right\}. \tag{14}$$

Substitution of χ into Eq. (12), performing the common variable transformation $x_d = x_1' - x_2'$ and $x_a = x_1' + x_2'$, and subsequent simplification yields

$$\begin{aligned} W^s\left(\boldsymbol{\rho}_1, \boldsymbol{\rho}_2\right) = & \frac{E_0^2 k_0^2 e^{\mathrm{j}k_0(\rho_2-\rho_1)}\mathscr{S}^{\perp}}{32\pi\rho_s\sqrt{\rho_1\rho_2\left(a^2-b^2\right)}}\exp\left[-\frac{k_0^2\sigma_h^2}{2}\left(\vartheta_{y1}^2+\vartheta_{y2}^2\right)\right] \\ & \int_{-2L}^{2L}\exp\left[-\frac{\left(\tilde{a}-\tilde{b}\right)k_0^2(\hat{\mathbf{x}}\cdot\hat{\mathbf{u}})^2}{2\rho_s^2}x_a^2\right]\exp\left[\mathrm{j}\frac{k_0}{2}\left(\vartheta_{x1}-\vartheta_{x2}\right)x_a\right] \\ & \int_{|x_a|-2L}^{2L-|x_a|}\exp\left[-\frac{\left(\tilde{a}+\tilde{b}\right)k_0^2(\hat{\mathbf{x}}\cdot\hat{\mathbf{u}})^2}{2\rho_s^2}x_d^2\right]\exp\left[k_0^2\sigma_h^2\vartheta_{y1}\vartheta_{y2}\exp\left(-\frac{x_d^2}{\ell_h^2}\right)\right] \\ & \exp\left[\mathrm{j}\frac{k_0}{2}\left(\vartheta_{x1}+\vartheta_{x2}\right)x_d\right]\exp\left[-\mathrm{j}\frac{k_0(\hat{\mathbf{x}}\cdot\hat{\mathbf{u}})^2x_a}{2\rho_s}x_d\right]\mathrm{d}x_d\mathrm{d}x_a \end{aligned} \tag{15}$$

#182849 - $15.00 USD Received 4 Jan 2013; revised 18 Feb 2013; accepted 4 Mar 2013; published 12 Mar 2013

At this point it is necessary to handle the exponential term containing the surface autocorrelation function. Classically, this has been done in one of two ways. The first is to expand the exponential term in a Taylor series and proceed with the evaluation of the integrals [23]. Mathematically, this approach is applicable to all surfaces; however, computationally (because the series is slowly convergent), this approach is limited to smooth-to-moderately rough surfaces and is investigated in the next section. The other approach involves expanding the surface autocorrelation function in a Taylor series and only retaining the first two terms, i.e., $\exp\left(-x_d^2/\ell_h^2\right) \approx 1 - x_d^2/\ell_h^2$ [3, 23]. This treatment is applicable to very rough surfaces and is discussed in Section 2.2.2.

2.2.1. Smooth-to-moderately rough surfaces

As briefly discussed in the previous section, further progress can be made on Eq. (15) by expanding the exponential term containing the surface autocorrelation function in a Taylor series, specifically,

$$\exp\left[k_0^2\sigma_h^2\vartheta_{y1}\vartheta_{y2}\exp\left(-\frac{x_d^2}{\ell_h^2}\right)\right] = \sum_{m=0}^{\infty}\frac{\left(k_0^2\sigma_h^2\vartheta_{y1}\vartheta_{y2}\right)^m}{m!}\exp\left(-\frac{mx_d^2}{\ell_h^2}\right). \tag{16}$$

Substitution of this series into Eq. (15) and subsequent evaluation of the integral over x_d results in

$$\begin{aligned} W^s(\boldsymbol{\rho}_1,\boldsymbol{\rho}_2) = {} & \frac{E_0^2k_0^2\ell_h e^{\mathrm{j}k_0(\rho_2-\rho_1)}\mathscr{S}^{\perp}}{16\sqrt{2\pi\rho_1\rho_2\left(a^2-b^2\right)}}\exp\left[-\frac{k_0^2\sigma_h^2}{2}\left(\vartheta_{y1}^2+\vartheta_{y2}^2\right)\right] \\ & \sum_{m=0}^{\infty}\frac{\left(k_0^2\sigma_h^2\vartheta_{y1}\vartheta_{y2}\right)^m}{m!}\frac{\exp\left[-\frac{k_0^2\ell_h^2\rho_s^2}{8\mathscr{D}_m}\left(\vartheta_{x1}+\vartheta_{x2}\right)^2\right]}{\sqrt{\mathscr{D}_m}} \\ & \int_{-2L}^{2L}\exp\left\{-\frac{k_0^2(\hat{\mathbf{x}}\cdot\hat{\mathbf{u}})^2x_a^2}{2}\left[\frac{\left(\tilde{a}-\tilde{b}\right)}{\rho_s^2}+\frac{\ell_h^2(\hat{\mathbf{x}}\cdot\hat{\mathbf{u}})^2}{4\mathscr{D}_m}\right]\right\} \\ & \exp\left\{\frac{k_0x_a}{2}\left[\frac{k_0\rho_2\ell_h^2(\hat{\mathbf{x}}\cdot\hat{\mathbf{u}})^2\left(\vartheta_{x1}+\vartheta_{x2}\right)}{2\mathscr{D}_m}+\mathrm{j}\left(\vartheta_{x1}-\vartheta_{x2}\right)\right]\right\} \\ & \mathrm{Re}\left\{\mathrm{erf}\left(\frac{(2L-|x_a|)\sqrt{\mathscr{D}_m}}{\sqrt{2}\rho_s\ell_h}+\mathrm{j}\frac{k_0\rho_s\ell_h}{2\sqrt{2\mathscr{D}_m}}\left[\frac{(\hat{\mathbf{x}}\cdot\hat{\mathbf{u}})^2}{\rho_s}x_a-\left(\vartheta_{x1}+\vartheta_{x2}\right)\right]\right)\right\}\mathrm{d}x_a \end{aligned}, \tag{17}$$

where $\mathscr{D}_m = k_0^2(\hat{\mathbf{x}}\cdot\hat{\mathbf{u}})^2\ell_h^2\left(\tilde{a}+\tilde{b}\right)+2m\rho_s^2$.

In order to evaluate the remaining integral and arrive at a closed-form solution, the complex error function (erf) must be properly handled. While it is possible to determine the order of the error function argument by using physical insight and examining the associated exponential functions in Eq. (17), it is much simpler to examine the integrand in Eq. (15) and determine the condition at which the x_d integration limits can be extended from $[|x_a|-2L, 2L-|x_a|]$ to $(-\infty,\infty)$. A necessary condition for this approximation occurs when

$$\exp\left\{-x_d^2\left[\frac{\left(\tilde{a}+\tilde{b}\right)k_0^2(\hat{\mathbf{x}}\cdot\hat{\mathbf{u}})^2}{2\rho_s^2}+\frac{m}{\ell_h^2}\right]\right\} > \delta, \tag{18}$$

where δ is a user-defined parameter and denotes the point at which the exponential function no longer has significant value. Taking note that the minimum of the exponential function's

#182849 - $15.00 USD Received 4 Jan 2013; revised 18 Feb 2013; accepted 4 Mar 2013; published 12 Mar 2013

argument occurs when $m=0$ and that the maximum value x_d takes on in the integration is $2L$, the following condition can be derived:

$$L > \frac{\rho_s}{k_0 w_s \sqrt{2}\,|\hat{\mathbf{x}}\cdot\hat{\mathbf{u}}|}\sqrt{-\ln\delta}. \tag{19}$$

The above condition physically means that the projected fully-coherent incident beam size must "fit" on the rough surface for the erf ≈ 1, or equivalently, the x_d integration limits in Eq. (15) $[|x_a|-2L, 2L-|x_a|] \approx (-\infty,\infty)$. How well the incident beam "fits" is determined by δ—the smaller the δ, the more accurate the approximation. If the projected fully-coherent incident beam size does not "fit" on the rough surface, the erf $\neq 1$ and the remaining expression must be evaluated numerically.

Assuming that the above condition holds, the remaining integral in Eq. (17) can be evaluated, namely,

$$\begin{aligned}
W^s(\boldsymbol{\rho}_1,\boldsymbol{\rho}_2) = {} & \frac{E_0^2 k_0 \ell_h \rho_s e^{\mathrm{j}k_0(\rho_2-\rho_1)}\mathscr{S}^{\perp}}{16\,|\hat{\mathbf{x}}\cdot\hat{\mathbf{u}}|\sqrt{\rho_1\rho_2\,(a^2-b^2)}}\exp\left[-\frac{k_0^2\sigma_h^2}{2}\left(\vartheta_{y1}^2+\vartheta_{y2}^2\right)\right] \\
& \sum_{m=0}^{\infty}\frac{\left(k_0^2\sigma_h^2\vartheta_{y1}\vartheta_{y2}\right)^m}{m!\sqrt{\mathscr{A}_m}}\exp\left[-\frac{k_0^2\rho_s^2\ell_h^2}{4\mathscr{D}_m}\left(1-\frac{\rho_s^2\ell_h^2(\hat{\mathbf{x}}\cdot\hat{\mathbf{u}})^2}{\mathscr{A}_m}\right)\left(\vartheta_{x1}^2+\vartheta_{x2}^2\right)\right] \\
& \exp\left\{-\frac{\rho_s^2\left[k_0^2\ell_h^2(\hat{\mathbf{x}}\cdot\hat{\mathbf{u}})^2\tilde{b}+m\rho_s^2\right]}{\mathscr{A}_m(\hat{\mathbf{x}}\cdot\hat{\mathbf{u}})^2}(\vartheta_{x1}-\vartheta_{x2})^2\right\}\exp\left[\mathrm{j}\frac{k_0\ell_h^2\rho_s^3}{2\mathscr{A}_m}\left(\vartheta_{x1}^2-\vartheta_{x2}^2\right)\right] \\
& \left\{\mathrm{erf}\left[\frac{Lk_0\,|\hat{\mathbf{x}}\cdot\hat{\mathbf{u}}|}{\rho_s}\sqrt{\frac{\mathscr{A}_m}{2\mathscr{D}_m}}+\frac{k_0\,|\hat{\mathbf{x}}\cdot\hat{\mathbf{u}}|\,\rho_s^2\ell_h^2}{2\sqrt{2\mathscr{D}_m\mathscr{A}_m}}(\vartheta_{x1}+\vartheta_{x2})+\mathrm{j}\frac{\rho_s}{|\hat{\mathbf{x}}\cdot\hat{\mathbf{u}}|}\sqrt{\frac{\mathscr{D}_m}{2\mathscr{A}_m}}(\vartheta_{x1}-\vartheta_{x2})\right]\right. \\
& \left.+\mathrm{erf}\left[\frac{Lk_0\,|\hat{\mathbf{x}}\cdot\hat{\mathbf{u}}|}{\rho_s}\sqrt{\frac{\mathscr{A}_m}{2\mathscr{D}_m}}-\frac{k_0\,|\hat{\mathbf{x}}\cdot\hat{\mathbf{u}}|\,\rho_s^2\ell_h^2}{2\sqrt{2\mathscr{D}_m\mathscr{A}_m}}(\vartheta_{x1}+\vartheta_{x2})-\mathrm{j}\frac{\rho_s}{|\hat{\mathbf{x}}\cdot\hat{\mathbf{u}}|}\sqrt{\frac{\mathscr{D}_m}{2\mathscr{A}_m}}(\vartheta_{x1}-\vartheta_{x2})\right]\right\}
\end{aligned}, \tag{20}$$

where $\mathscr{A}_m = 4\mathscr{D}_m\left(\tilde{a}-\tilde{b}\right)+\rho_s^2\ell_h^2(\hat{\mathbf{x}}\cdot\hat{\mathbf{u}})^2$. A similar analysis to that performed above can be performed for the error functions in this expression. The condition for the sum of the erf's ≈ 2 is

$$L > \frac{\rho_s\sqrt{1+(2/\alpha)^2}}{k_0 w_s\sqrt{2}\,|\hat{\mathbf{x}}\cdot\hat{\mathbf{u}}|}\sqrt{-\ln\delta}, \tag{21}$$

where $\alpha=\ell_s/w_s$. This condition physically means that the projected partially-coherent beam size must "fit" on the rough surface in order to safely assume that the sum of the erf's ≈ 2. This condition is more stringent than Eq. (19).

The physical interpretation of Eq. (20) is obscured somewhat by the summation; however, the exponential term on the second line of the expression generally drives the angular extent of the scattered SD. The first exponential term on the third line generally determines the angular extent over which the scattered field is correlated, i.e., the SDoC radius. The SD S and SDoC μ definitions can be found in Refs. [33, 35, 36]. When one considers a fully-coherent incident Gaussian beam ($\ell_s\to\infty$) and quasi-monochromatic light [58], the coherent scattered irradiance, i.e., $I_c^s=\left|\langle E_z^s\rangle\right|^2$, can be determined quite easily from Eq. (20) by considering just the $m=0$ term of the series and setting $\boldsymbol{\rho}_1=\boldsymbol{\rho}_2=\boldsymbol{\rho}$. With some minor algebraic manipulation, one arrives at the two-dimensional form of the coherent scattered irradiance expression derived by Wang *et al.* [2]. One can also derive from Eq. (20) the incoherent scattered irradiance I_i^s for a fully-coherent incident Gaussian beam and quasi-monochromatic light. Note that I_i^s is

#182849 - $15.00 USD Received 4 Jan 2013; revised 18 Feb 2013; accepted 4 Mar 2013; published 12 Mar 2013

equivalent to the variance of the scattered field, i.e., $I_i^s = I^s - I_c^s$, where $I^s = \left\langle E_z^s E_z^{s*} \right\rangle$ is the average scattered irradiance. This expression also simplifies to the form derived by Wang *et al.* [2].

2.2.2. Very rough surfaces

Consider the form of the joint characteristic function:

$$\begin{aligned}\chi &= \exp\left[-\frac{k_0^2\sigma_h^2}{2}\left(\vartheta_{y1}^2+\vartheta_{y2}^2\right)\right]\exp\left[k_0^2\sigma_h^2\vartheta_{y1}\vartheta_{y2}\exp\left(-\frac{x_d^2}{\ell_h^2}\right)\right] \\ &= \exp\left\{-\frac{k_0^2\sigma_h^2}{2}\vartheta_{y1}\vartheta_{y2}\left[\frac{\vartheta_{y1}}{\vartheta_{y2}}+\frac{\vartheta_{y2}}{\vartheta_{y1}}-2\exp\left(-\frac{x_d^2}{\ell_h^2}\right)\right]\right\}\end{aligned}. \tag{22}$$

In the case of very rough surfaces, i.e., $k_0^2\sigma_h^2\vartheta_{y1}\vartheta_{y2}/2 \gg 1$, χ only has significant value when $\vartheta_{y1}/\vartheta_{y2}+\vartheta_{y2}/\vartheta_{y1}-2\exp\left(-x_d^2/\ell_h^2\right)\approx 0$. Considering that $\vartheta_{y1}/\vartheta_{y2}\approx\vartheta_{y2}/\vartheta_{y1}$, $\vartheta_{y1}/\vartheta_{y2}+\vartheta_{y2}/\vartheta_{y1}-2\exp\left(-x_d^2/\ell_h^2\right)\approx 0$ is only possible for small x_d. Thus, it makes sense to expand $\exp\left(-x_d^2/\ell_h^2\right)$ and retain the first two terms, i.e., $\exp\left(-x_d^2/\ell_h^2\right)\approx 1-x_d^2/\ell_h^2$. Substituting this into Eq. (15) and carrying out the integrations, one arrives at the desired result for the scattered field CSD function:

$$\begin{aligned}W^s(\boldsymbol{\rho}_1,\boldsymbol{\rho}_2) &= \frac{E_0^2 k_0\ell_h\rho_s e^{\mathrm{j}k_0(\rho_2-\rho_1)}\mathscr{S}^\perp}{16\left|\hat{\mathbf{x}}\cdot\hat{\mathbf{u}}\right|\sqrt{\rho_1\rho_2\left(a^2-b^2\right)}}\exp\left[-\frac{k_0^2\sigma_h^2}{2}\left(\vartheta_{y1}-\vartheta_{y2}\right)^2\right]\frac{1}{\sqrt{\tilde{\mathscr{A}}}} \\ &\exp\left[-\frac{k_0^2\rho_s^2\ell_h^2}{4\tilde{\mathscr{D}}}\left(1-\frac{\rho_s^2\ell_h^2\left(\hat{\mathbf{x}}\cdot\hat{\mathbf{u}}\right)^2}{\tilde{\mathscr{A}}}\right)\left(\vartheta_{x1}^2+\vartheta_{x2}^2\right)\right]\exp\left[\mathrm{j}\frac{k_0\ell_h^2\rho_s^3}{2\tilde{\mathscr{A}}}\left(\vartheta_{x1}^2-\vartheta_{x2}^2\right)\right] \\ &\exp\left\{-\frac{k_0^2\rho_s^2\left[\ell_h^2\left(\hat{\mathbf{x}}\cdot\hat{\mathbf{u}}\right)^2\tilde{b}+\sigma_h^2\rho_s^2\vartheta_{y1}\vartheta_{y2}\right]}{\tilde{\mathscr{A}}\left(\hat{\mathbf{x}}\cdot\hat{\mathbf{u}}\right)^2}\left(\vartheta_{x1}-\vartheta_{x2}\right)^2\right\} \\ &\left\{\mathrm{erf}\left[\frac{Lk_0\left|\hat{\mathbf{x}}\cdot\hat{\mathbf{u}}\right|}{\rho_s}\sqrt{\frac{\tilde{\mathscr{A}}}{2\tilde{\mathscr{D}}}}+\frac{k_0\left|\hat{\mathbf{x}}\cdot\hat{\mathbf{u}}\right|\rho_s^2\ell_h^2}{2\sqrt{2\tilde{\mathscr{D}}\tilde{\mathscr{A}}}}\left(\vartheta_{x1}+\vartheta_{x2}\right)+\mathrm{j}\frac{\rho_s}{\left|\hat{\mathbf{x}}\cdot\hat{\mathbf{u}}\right|}\sqrt{\frac{\tilde{\mathscr{D}}}{2\tilde{\mathscr{A}}}}\left(\vartheta_{x1}-\vartheta_{x2}\right)\right]\right. \\ &\left.+\mathrm{erf}\left[\frac{Lk_0\left|\hat{\mathbf{x}}\cdot\hat{\mathbf{u}}\right|}{\rho_s}\sqrt{\frac{\tilde{\mathscr{A}}}{2\tilde{\mathscr{D}}}}-\frac{k_0\left|\hat{\mathbf{x}}\cdot\hat{\mathbf{u}}\right|\rho_s^2\ell_h^2}{2\sqrt{2\tilde{\mathscr{D}}\tilde{\mathscr{A}}}}\left(\vartheta_{x1}+\vartheta_{x2}\right)-\mathrm{j}\frac{\rho_s}{\left|\hat{\mathbf{x}}\cdot\hat{\mathbf{u}}\right|}\sqrt{\frac{\tilde{\mathscr{D}}}{2\tilde{\mathscr{A}}}}\left(\vartheta_{x1}-\vartheta_{x2}\right)\right]\right\}\end{aligned}, \tag{23}$$

where $\tilde{\mathscr{D}} = k_0^2\left(\hat{\mathbf{x}}\cdot\hat{\mathbf{u}}\right)^2\ell_h^2\left(\tilde{a}+\tilde{b}\right)+2k_0^2\sigma_h^2\vartheta_{y1}\vartheta_{y2}\rho_s^2$ and $\tilde{\mathscr{A}} = 4\tilde{\mathscr{D}}\left(\tilde{a}-\tilde{b}\right)+\rho_s^2\ell_h^2\left(\hat{\mathbf{x}}\cdot\hat{\mathbf{u}}\right)^2$. If Eq. (21) is satisfied, then the sum of the erf's ≈ 2.

The above expression for the scattered field CSD function is remarkably physical. The first exponential term on the second line of Eq. (23) is predominately responsible for the angular extent of the scattered SD. This exponential term is a function of the sum of the squares of the projected observation angles ϑ_{x1} and ϑ_{x2}. The exponential term on the third line of Eq. (23) determines the SDoC radius. Note that this term is a function of the difference of the projected observation angles, i.e., $|\vartheta_{x1}-\vartheta_{x2}| = |\sin\theta_1^r - \sin\theta_2^r|$. Thus, it could be stated that the scattered field CSD function maintains its GSM form with respect to ϑ_{x1} and ϑ_{x2} if Eq. (21) is satisfied.

Because of the magnitude of the argument of the "correlation" exponential (specifically, the $k_0^2\rho_s^4\sigma_h^2\vartheta_{y1}\vartheta_{y2}$ term), $\sin\theta_1^r \approx \sin\theta_2^r$, implying that $\theta_1^r \approx \theta_2^r$, for the exponential to have a significant value. This implies that the correlation exponential is approximately a function of $\Delta\theta^r = \theta_1^r - \theta_2^r$. Since this term is predominately responsible for the behavior of the SDoC, the SDoC is also a function (approximately) of $\Delta\theta^r = \theta_1^r - \theta_2^r$. This is in agreement with the findings of previous studies which were restricted to the paraxial regime.

#182849 - $15.00 USD Received 4 Jan 2013; revised 18 Feb 2013; accepted 4 Mar 2013; published 12 Mar 2013

2.3. Angular spectral degree of coherence radius

In this section, a theoretical form for the angular SDoC radius is derived from Eq. (23). Note that because of the summation in Eq. (20), it is not possible to derive an expression for the angular SDoC radius using that form of the scattered field CSD function.

Assuming Eq. (21) is satisfied and setting the exponential term on line three of Eq. (23) equal to $1/e$ results in the following expression:

$$\begin{aligned} |\vartheta_{x1}-\vartheta_{x2}|_{1/e} &= |\sin\theta_1^r-\sin\theta_2^r|_{1/e} \\ &\approx \frac{|\hat{\mathbf{x}}\cdot\hat{\mathbf{u}}|}{\rho_s}\sqrt{8\frac{w_s^2\ell_s^2}{\ell_s^2+4w_s^2}+\frac{2\rho_s^2\ell_h^2(\hat{\mathbf{x}}\cdot\hat{\mathbf{u}})^2}{k_0^2}\frac{1}{\ell_h^2w_s^2(\hat{\mathbf{x}}\cdot\hat{\mathbf{u}})^2+2\rho_s^2\sigma_h^2\vartheta_{y1}\vartheta_{y2}}}. \end{aligned} \tag{24}$$

As discussed above, the magnitude of the argument of the correlation exponential term is very large; thus, $\theta_1^r\approx\theta_2^r$ for the correlation term to have a significant value. Note that this physically implies that the scattered field is correlated for observation points separated by very small angles. The fact that $\theta_1^r\approx\theta_2^r$ motivates setting $\theta_1^r=\theta_2^r+\Delta\theta^r$ and expanding $\sin\theta_1^r$ in a Taylor series about $\theta_2^r=\theta^r$. After some simple algebra, the expression for the angular SDoC radius becomes

$$\begin{aligned} |\Delta\theta^r|_{1/e} &\approx \frac{\cos\theta^i}{\rho_s\cos\theta^r} \\ &\sqrt{8\frac{w_s^2\ell_s^2}{\ell_s^2+4w_s^2}+\frac{2}{k_0^2}\frac{1}{\sigma_{h'}^2(1+\cos\theta^r/\cos\theta^i)^2}\frac{1}{1+\left[\frac{\Omega}{\sigma_{h'}(1+\cos\theta^r/\cos\theta^i)}\right]^2}}, \end{aligned} \tag{25}$$

where $\alpha=\ell_s/w_s$ (previously defined), $\Omega=w_s/\rho_s$ is the half-angle subtended by the source viewed from the rough surface, and $\sigma_{h'}=\sqrt{2}\sigma_h/\ell_h$ is the surface slope standard deviation [22, 23]. Note that the same procedure applied to ϑ_{x1} and ϑ_{x2} (discussed above) has been applied to ϑ_{y1} and ϑ_{y2} in deriving the above expression.

The term involving Ω and $\sigma_{h'}$ can be neglected when one considers that typical values for these parameters range from approximately 10^{-4} rad and 0.05–0.5 rad, respectively. Note that the first term under the radical contains only source parameters, while the second term contains mostly rough surface parameters. In many scenarios of interest the source term is much greater than the rough surface term; thus, factoring out the source term and expanding the resulting radical in a Taylor series yields

$$|\Delta\theta^r|_{1/e}\approx 2\Omega\sqrt{\frac{2}{1+(2/\alpha)^2}}\frac{\cos\theta^i}{\cos\theta^r}+\frac{\Omega\sqrt{2}}{k_0^2w_s^2}\frac{\sqrt{1+(2/\alpha)^2}}{4\sigma_{h'}^2(1+\cos\theta^r/\cos\theta^i)^2}\frac{\cos\theta^i}{\cos\theta^r}. \tag{26}$$

The first term is entirely composed of source parameters and therefore represents the source contribution to the angular SDoC radius. Because of the presence of $\sigma_{h'}$, the second term provides a small correction to the angular SDoC radius due to the roughness of the surface. In most cases, the angular SDoC radius can be safely approximated by utilizing only the first term making the expression dependent only on the properties of the source illumination. This is consistent with the classic narrow-band, fully-coherent result derived by Goodman [26]. Note that when $\theta^r\approx\theta^i$, i.e., when observation is in the specular direction, the dependence of the expression on observation and incident angles disappears.

#182849 - $15.00 USD Received 4 Jan 2013; revised 18 Feb 2013; accepted 4 Mar 2013; published 12 Mar 2013

2.4. Angular spectral density radius

As is the case with the angular SDoC radius, an expression for the angular SD radius can only be derived using the very rough surface form of the scattered field CSD function in Eq. (23). Furthermore, the expression can only be derived for near-normal incidence.

Assuming Eq. (21) is satisfied, letting $\theta^i = 0$ and $\theta_1^r = \theta_2^r = \theta_{1/e}^r$, and setting the first exponential term on line two of Eq. (23) equal to $1/e$ yields the following expression after some simplification:

$$\sin^2\theta_{1/e}^r = 2\Omega^2 + 2\sigma_{h'}^2\left(1+\cos\theta_{1/e}^r\right)^2 + \frac{1+(2/\alpha)^2}{2k_0^2w_s^2}, \tag{27}$$

where all symbols have been previously defined. With liberal use of trigonometric identities and some algebra, one arrives at

$$\cos^4\left(\theta_{1/e}^r/2\right) - \frac{1}{1+2\sigma_{h'}^2}\cos^2\left(\theta_{1/e}^r/2\right) + \frac{2\Omega^2 + \frac{1+(2/\alpha)^2}{2k_0^2w_s^2}}{4+8\sigma_{h'}^2} = 0. \tag{28}$$

One quickly recognizes that the above expression is a quadratic equation in terms of $\cos^2\left(\theta_{1/e}^r/2\right)$. Letting $\psi = \cos^2\left(\theta_{1/e}^r/2\right)$, implying that $\theta_{1/e}^r = 2\cos^{-1}\sqrt{\psi}$ (only the positive ψ root makes physical sense), and utilizing the quadratic formula, yields the following roots for ψ:

$$\psi = \frac{1}{2+4\sigma_{h'}^2}\left[1 \pm \sqrt{1-\left(1+2\sigma_{h'}^2\right)\left(2\Omega^2 + \frac{1+(2/\alpha)^2}{2k_0^2w_s^2}\right)}\right]. \tag{29}$$

The second term in the radicand is much less than one; therefore, only the "plus" root has significant value. Choosing the "plus" root, expanding the radical in a Taylor series, and applying $\theta_{1/e}^r = 2\cos^{-1}\sqrt{\psi}$ produces

$$\begin{aligned}\theta_{1/e}^r &\approx 2\cos^{-1}\left[\sqrt{\frac{1}{1+2\sigma_{h'}^2}}\sqrt{1-\frac{1}{4}\left(1+2\sigma_{h'}^2\right)\left(2\Omega^2+\frac{1+(2/\alpha)^2}{2k_0^2w_s^2}\right)}\right] \\ &\approx 2\cos^{-1}\left[\sqrt{\frac{1}{1+2\sigma_{h'}^2}} - \frac{1}{8}\sqrt{1+2\sigma_{h'}^2}\left(2\Omega^2+\frac{1+(2/\alpha)^2}{2k_0^2w_s^2}\right)\right]\end{aligned}. \tag{30}$$

In Eq. (30), the first term in the argument of the inverse cosine depends solely on the characteristics of the rough surface and it physically represents the rough surface contribution to the angular extent of the SD. The second argument contains terms dealing with the source parameters and provides a small correction to the angular SD radius due to the size and coherence of the source. In most cases, the angular SD radius can be approximated using only the first term making the expression solely dependent on the roughness of the surface.

2.5. Parallel-polarization cross-spectral density function

Considering that the rough surface's features are large compared to wavelength, intuition dictates that the p-pol scattered field should have the same general behavior as the s-pol scattered field. This is the case. The only difference between the s-pol and p-pol CSD functions is the parameter $\mathscr{S}$. Setting $\mathscr{S}^\perp = \mathscr{S}^\parallel$ in Eqs. (20) and (23) yields the p-pol scattered field CSD functions. Expressions for $\mathscr{S}^\parallel$ and $\mathscr{S}^\perp$ can be found in the appendix.

#182849 - $15.00 USD Received 4 Jan 2013; revised 18 Feb 2013; accepted 4 Mar 2013; published 12 Mar 2013

3. Validation of analytical solutions

In this section, the analytical solutions for the scattered field CSD functions derived above are validated via experiments, full-wave electromagnetic simulations, and PO simulations. For the experimental validation, the Complete Angle Scatter Instrument (CASI) [60] at the Air Force Institute of Technology was used. Measurements of the scattered SD S^s versus θ^r from a LabSphere Infragold [61] 5.08 cm $\times$ 5.08 cm coupon were made at $\lambda = 3.39$ μm (HeNe MWIR laser) and $\theta^i = 20^\circ$, 40°, and 60°. Before the scattering measurements were made, the surface statistics of the Infragold coupon were determined using a KLA Tencor Alpha-Step IQ surface profiler [62]. Four 1 cm scans (step size 0.2 μm), performed along different directions, were taken and analyzed. The measured surface height standard deviation σ_h, surface slope standard deviation $\sigma_{h'}$, and correlation length ℓ_h were 11.09 μm, 0.2441 rad, and 116.9 μm, respectively.

For the full-wave electromagnetic simulations, the Method of Moments (MoM) [63] was used to solve the following impedance-boundary-condition-based s-pol electric field integral equation for the unknown electric current $\mathbf{J}$:

$$E_z^i(\boldsymbol{\rho}) = \sqrt{\frac{\mu}{\varepsilon}} J_z(\boldsymbol{\rho}) + \mathrm{j}k_0 \sqrt{\frac{\mu_0}{\varepsilon_0}} A_z(\boldsymbol{\rho}) + \left(\frac{\partial F_y(\boldsymbol{\rho})}{\partial x} - \frac{\partial F_x(\boldsymbol{\rho})}{\partial y} \right) \quad \boldsymbol{\rho} \in C, \tag{31}$$

where $\mathbf{A}$ and $\mathbf{F}$ are the magnetic and electric vector potentials, respectively [64]. Once $\mathbf{J}$ had been found, the scattered field was determined via convolution with the far-field form of the free-space Green's function. A narrow-band, fully-coherent Gaussian beam was used for the incident field E_z^i. S^s versus θ^r and the modulus of the SDoC $|\mu^s|$ versus $\Delta\theta^r$ were calculated using the scattered field predicted from 500 rough surface realizations at $\lambda = 3.39$ μm, the Infragold surface statistics stated above, and a complex index of refraction $n - \mathrm{j}\kappa$ for gold of $1.995 - \mathrm{j}20.95$ [65]. The 500 rough surface realizations were generated using the method outlined by Yura and Hanson [66].

Both the experimental and full-wave simulations used narrow-band, fully-coherent incident fields. To verify the predictions of the analytical solutions for partially-coherent incident fields, PO Monte Carlo simulations were also performed. To model the random nature of the incident field, 500 source plane field instances were generated using the phase screen method described by Xiao and Voelz [67]. For the random surface, 500 rough surface instances were generated using the technique detailed in Ref. [66]. The 500 source plane field instances were propagated to and evaluated at each rough surface instance. The scattered fields were then computed numerically using the relations in Eq. (5). The end result of this process was a set of 500^2 scattered fields, from which $|\mu^s|$ and S^s were computed. These simulations were performed at $\lambda = 3.39$ μm using hypothetical rough aluminum surfaces $n - \mathrm{j}\kappa = 5.366 - \mathrm{j}33.33$ [65] with varying degrees of surface roughness. In addition, the properties of the incident field (size and coherence) were also varied to examine their effects.

3.1. Results

Figure 2 shows the normalized S^s CASI measurement, MoM simulation, PO analytical solution, and PO simulation results versus θ^r. The simulations were setup to best match the CASI experimental scenario, i.e., $\rho_s = 185$ cm and $w_s \approx 0.5$ mm. For MoM computational reasons, $L = 2.5$ mm, which resulted in an incident beam which over-illuminated the rough surface by less than 2%. While all the traces possess a Gaussian-like shape, there is a significant difference between the measured and MoM trace widths versus the PO results. As briefly discussed in Section 2.2, previous work had found that the SE-SE model more accurately represented surfaces roughened by random industrial processes [57]. If the Infragold sample measured and analyzed here adhered to the G-G model of rough surfaces, $\sigma_{h'} = \sqrt{2}\sigma_h/\ell_h \approx 0.1342$ rad. The

#182849 - $15.00 USD Received 4 Jan 2013; revised 18 Feb 2013; accepted 4 Mar 2013; published 12 Mar 2013

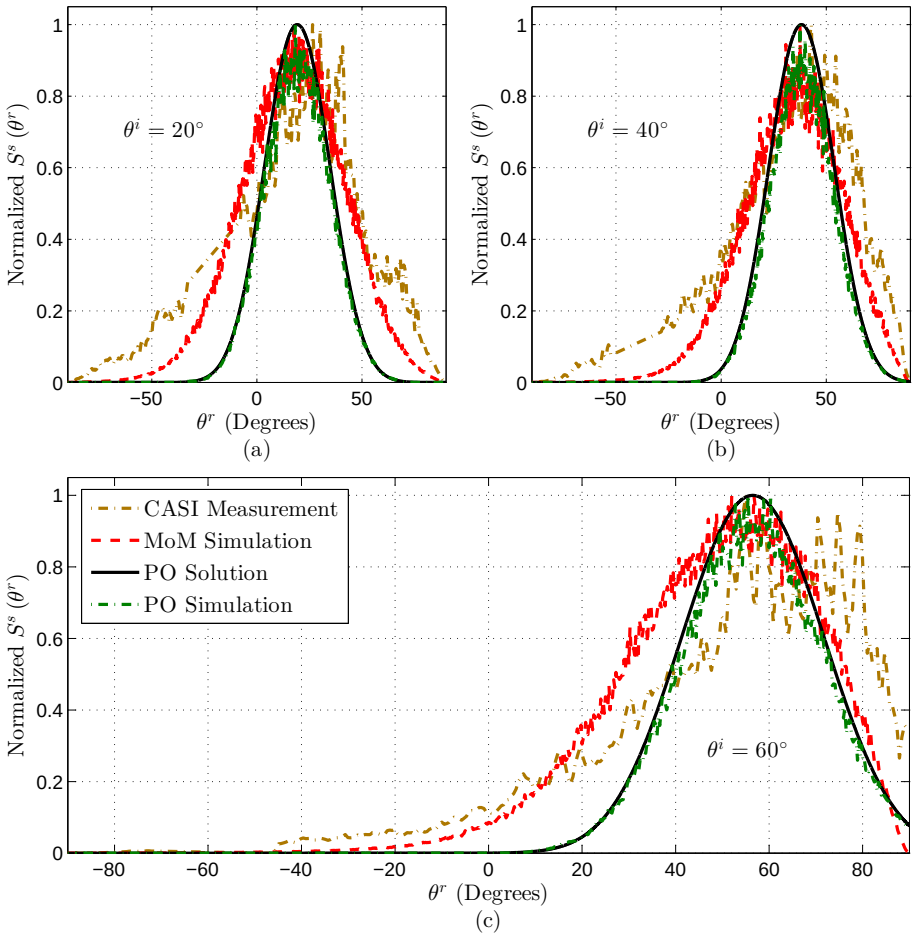

Fig. 2. CASI measurement, MoM simulation, analytical PO solution, and PO simulation results of normalized S^s versus θ^r for Infragold—(a) $\theta^i = 20°$, (a) $\theta^i = 40°$, and (c) $\theta^i = 60°$.

measured $\sigma_{h'}$ was roughly twice that value. Thus, in this case, the G-G model is not an ideal choice. Note that in these MoM simulation results, SE-SE surfaces were used, hence the good agreement with the CASI results. SE-SE surfaces could have been used in the PO simulations; however, as discussed previously, it would not have been possible to present analytical results. These results are presented for two main reasons. The first is to verify the analytical solutions which, based on the excellent agreement between the PO simulation and PO analytical results, is clearly accomplished. The other is to demonstrate the validity of the ubiquitous G-G model of rough surfaces. As can be seen, the model tends to underpredict the width of the scattered SD. Nevertheless, considering that analytical scattering solutions are possible using the G-G model, this is likely an acceptable drawback.

To truly validate the PO analytical solutions, MoM simulations were also performed using hypothetical Infragold G-G surfaces. These results, along with PO simulation and PO analytical solution results, are shown in Fig. 3. The source distance ρ_s, source radius w_s, and surface 1/2 length L were the same as above. The figure reports the normalized S^s versus θ^r in Fig. 3(a) and

#182849 - $15.00 USD Received 4 Jan 2013; revised 18 Feb 2013; accepted 4 Mar 2013; published 12 Mar 2013

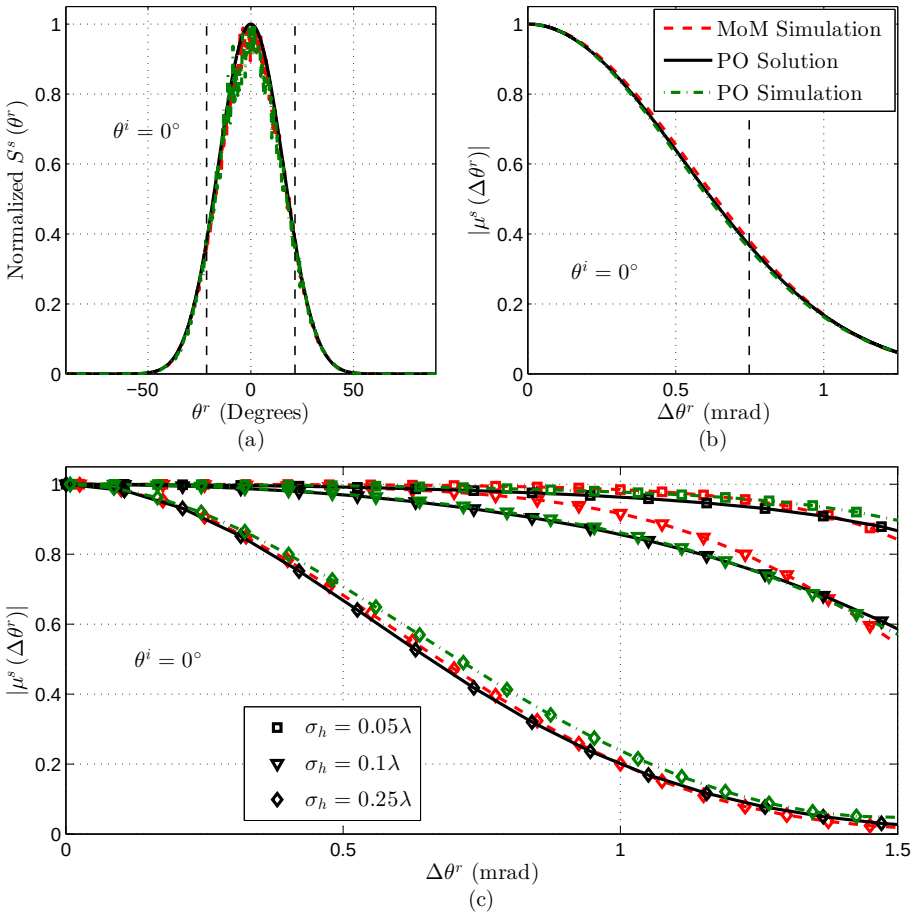

Fig. 3. MoM simulation, analytical PO solution, and PO simulation results of normalized S^s versus θ^r [(a)] and $|\mu^s|$ versus $\Delta\theta^r$ [(b) and (c)] for hypothetical Infragold G-G surfaces. In (a) and (b), the hypothetical Infragold surface possessed the measured σ_h and ℓ_h values of 11.09 μm and 116.9 μm, respectively. Since this hypothetical surface qualifies as a very rough surface, $\theta^r_{1/e}$ and $|\Delta\theta^r|_{1/e}$, given in Eqs. (30) and (26), are also plotted as vertical dashed line in (a) and (b), respectively. In (c), σ_h is varied while ℓ_h is held constant at 8λ.

$|\mu^s|$ versus $\Delta\theta^r$ in Figs. 3(b) and 3(c). In Figs. 3(a) and 3(b), the simulated Infragold surface possessed the same σ_h and ℓ_h values reported above. Since this hypothetical surface qualifies as a very rough surface, the theoretical angular SD and SDoC radii, given in Eqs. (30) and (26), respectively, are also plotted as vertical dashed line in Figs. 3(a) and 3(b). Note the excellent agreement between the MoM simulation, PO simulation, and analytical PO solution results. In Fig. 3(c), $|\mu^s|$ is shown for hypothetical Infragold G-G surfaces which possessed $\sigma_h = 0.05\lambda$, 0.1λ, and 0.25λ with ℓ_h held constant at 8λ. Surfaces with these parameters do not qualify as very rough surfaces and therefore, the angular SDoC radii are not shown. Again, note the very good agreement among the results.

Having validated the PO analytical solutions (as well as the PO simulation procedure) via experiment and full-wave electromagnetic simulations which utilized narrow-band, fully-coherent incident fields, attention can now be turned to validating the PO solutions via PO simulations

#182849 - $15.00 USD Received 4 Jan 2013; revised 18 Feb 2013; accepted 4 Mar 2013; published 12 Mar 2013

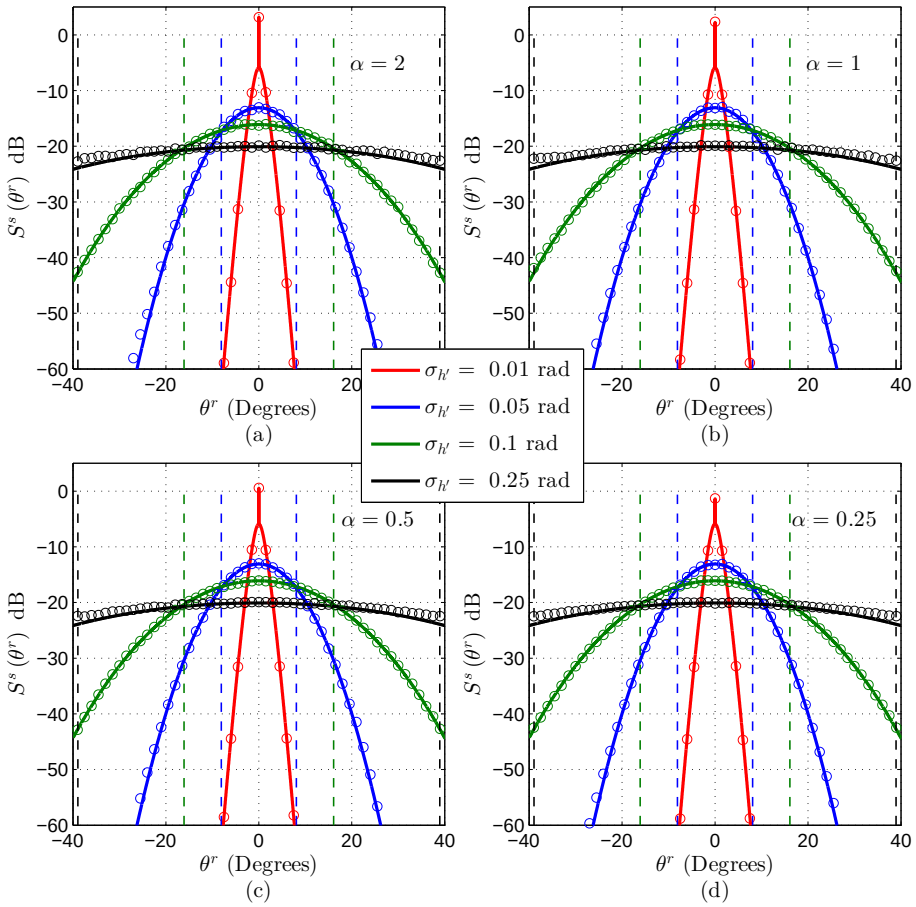

Fig. 4. S^s versus θ^r at normal incidence, i.e., $\theta^i = 0°$—(a) $\alpha = 2$, (b) $\alpha = 1$, (c) $\alpha = 0.5$, and (d) $\alpha = 0.25$. The solid traces are the PO analytical predictions, i.e., Eq. (20) or Eq. (23) (whichever is applicable); the circles are the PO simulation results. The vertical dashed lines in the figures mark the locations of $\theta^r_{1/e}$, namely, Eq. (30).

using partially-coherent incident fields. These results are reported in Figs. 4 and 5. Figure 4 shows the theoretical (solid curves) and simulated (circles) S^s for $\sigma_{h'} = 0.01$ rad, 0.05 rad, 0.1 rad, and 0.25 rad (with $\ell_h = 20\lambda$, $\sigma_h = \ell_h \sigma_{h'}/\sqrt{2}$, and $L = 0.35$ m) versus θ^r at normal incidence. Figures 4(a)–4(d) depict these curves for $\alpha = 2$, 1, 0.5, and 0.25 (with $w_s = 5$ mm), respectively, i.e., a coherent source to a relatively incoherent source. The vertical dashed lines in the figures mark the locations of $\theta^r_{1/e}$ given by Eq. (30). Note the excellent agreement between the simulated and theoretical predictions. Also note that although the coherence properties of the source are very different for the curves plotted in the figures, the S^s for the very rough surface curves $\sigma_{h'} = 0.05$ rad, 0.1 rad, and 0.25 rad are nearly identical. This physically implies that S^s (or the angular spread of the spectral density) for very rough surfaces is driven by surface properties not source parameters. Recall that this was theoretically predicted.

Figure 5 shows the theoretical (solid traces) and simulated (circles) $|\mu^s|$ for $\alpha = 2$, 1, 0.5, and 0.25 (with the same w_s as above) versus $\Delta\theta^r$. Figures 5(a)–5(d) show these curves for $\sigma_{h'} =$ 0.01 rad, 0.05 rad, 0.1 rad, and 0.25 rad (with the same ℓ_h, σ_h, and L as above), respectively,

#182849 - $15.00 USD Received 4 Jan 2013; revised 18 Feb 2013; accepted 4 Mar 2013; published 12 Mar 2013

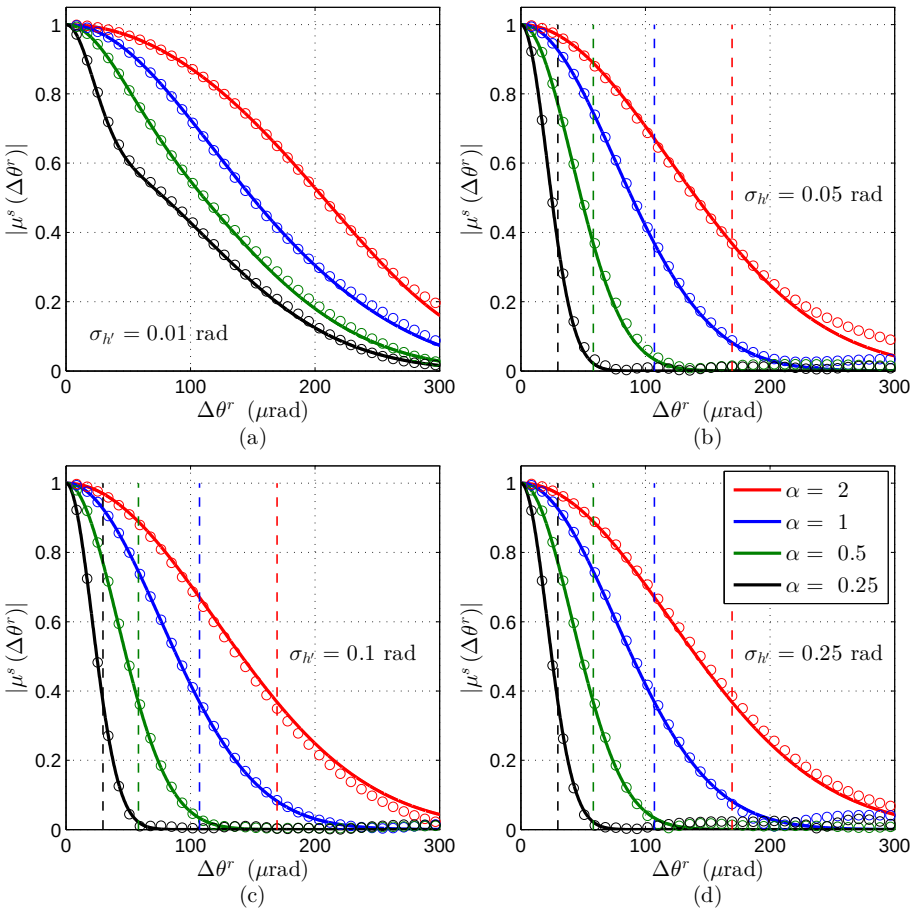

Fig. 5. $|\mu^s|$ versus $\Delta\theta^r$—(a) $\sigma_{h'} = 0.01$ rad, (b) $\sigma_{h'} = 0.05$ rad, (c) $\sigma_{h'} = 0.1$ rad, and (d) $\sigma_{h'} = 0.25$ rad. The solid traces are the PO analytical predictions, i.e., Eq. (20) or Eq. (23) (whichever is applicable); the circles are the PO simulation results. The vertical dashed lines in the figures mark the locations of $|\Delta\theta^r|_{1/e}$, namely, Eq. (26).

i.e., a smooth surface to a very rough surface. The vertical dashed lines in the figures mark the locations of $|\Delta\theta^r|_{1/e}$ given by Eq. (26). Recall that Eq. (26) is applicable to very rough surfaces, a condition not met by the surfaces whose results are shown in Fig. 5(a). Note the excellent agreement between the Monte Carlo simulation results and the theoretical predictions. Also note that $|\Delta\theta^r|_{1/e}$ depend almost exclusively on the coherence properties of the source α, as predicted.

4. Conclusion

The scattering of a partially-coherent field from a statistically rough surface was investigated. This work significantly extended previous efforts by incorporating the effects of material parameters (ε and μ) in the analysis and by rigorously validating the derived solutions via experiment and extensive simulation. Two forms of the scattered-field CSD function were derived in this work using the PO approximation. The first, applicable to smooth-to-moderately rough surfaces, was represented as an infinite series. While being a rather complicated expression

#182849 - $15.00 USD Received 4 Jan 2013; revised 18 Feb 2013; accepted 4 Mar 2013; published 12 Mar 2013

dependent on both source and surface parameters, physical insight was gleaned from its analytical form. The second form of the scattered field CSD function was applicable to very rough surfaces. This expression was examined at length to include derivations of the angular SDoC and SD radii. It was noted that under certain circumstances, this form of the CSD function maintained a GSM form in agreement with published results valid only in the paraxial regime. Lastly, the closed-form expressions for the scattered field CSD functions were rigorously validated with scatterometer measurements, as well as, MoM and PO Monte Carlo simulations. The analytical predictions were found to be in good agreement with the measurement and simulation results.

Appendix

The symbols first used in Eq. (12) are

$$\begin{aligned} \mathscr{S}^{\perp} &= \mathscr{H}_{\perp 1}\mathscr{H}_{\perp 2}^{*} \\ \mathscr{H}_{\perp 1,2} &= \left(\hat{\mathbf{x}}\cdot\hat{\mathbf{u}} - \frac{\vartheta_{x1,2}}{\vartheta_{y1,2}}\hat{\mathbf{y}}\cdot\hat{\mathbf{u}} + \hat{\mathbf{y}}\cdot\hat{\boldsymbol{\rho}}_{1,2} + \frac{\vartheta_{x1,2}}{\vartheta_{y1,2}}\hat{\mathbf{x}}\cdot\hat{\boldsymbol{\rho}}_{1,2}\right), \\ & -r_{\perp 1,2}\left(\hat{\mathbf{x}}\cdot\hat{\mathbf{u}} - \frac{\vartheta_{x1,2}}{\vartheta_{y1,2}}\hat{\mathbf{y}}\cdot\hat{\mathbf{u}} - \hat{\mathbf{y}}\cdot\hat{\boldsymbol{\rho}}_{1,2} - \frac{\vartheta_{x1,2}}{\vartheta_{y1,2}}\hat{\mathbf{x}}\cdot\hat{\boldsymbol{\rho}}_{1,2}\right) \end{aligned} \tag{32}$$

where

$$\begin{aligned} \vartheta_{x1,2} &= \hat{\mathbf{x}}\cdot\hat{\boldsymbol{\rho}}_{1,2} - \hat{\mathbf{x}}\cdot\hat{\mathbf{v}} \quad \vartheta_{y1,2} = \hat{\mathbf{y}}\cdot\hat{\boldsymbol{\rho}}_{1,2} - \hat{\mathbf{y}}\cdot\hat{\mathbf{v}} \\ a &= \frac{1}{4w_s^2} + \frac{1}{2\ell_s^2} \qquad b = \frac{1}{2\ell_s^2} \\ \tilde{a} &= \frac{a}{4\left(a^2 - b^2\right)} \qquad \tilde{b} = \frac{b}{4\left(a^2 - b^2\right)} \end{aligned} \quad . \tag{33}$$

For the p-pol case,

$$\begin{aligned} \mathscr{S}^{\parallel} &= \mathscr{H}_{\parallel 1}\mathscr{H}_{\parallel 2}^{*} \\ \mathscr{H}_{\parallel 1,2} &= \left(\hat{\mathbf{y}}\cdot\hat{\boldsymbol{\rho}}_{1,2} + \frac{\vartheta_{x1,2}}{\vartheta_{y1,2}}\hat{\mathbf{x}}\cdot\hat{\boldsymbol{\rho}}_{1,2} - \hat{\mathbf{x}}\cdot\hat{\mathbf{u}} + \frac{\vartheta_{x1,2}}{\vartheta_{y1,2}}\hat{\mathbf{y}}\cdot\hat{\mathbf{u}}\right), \\ & -r_{\parallel 1,2}\left(\hat{\mathbf{y}}\cdot\hat{\boldsymbol{\rho}}_{1,2} + \frac{\vartheta_{x1,2}}{\vartheta_{y1,2}}\hat{\mathbf{x}}\cdot\hat{\boldsymbol{\rho}}_{1,2} + \hat{\mathbf{x}}\cdot\hat{\mathbf{u}} - \frac{\vartheta_{x1,2}}{\vartheta_{y1,2}}\hat{\mathbf{y}}\cdot\hat{\mathbf{u}}\right) \end{aligned} \tag{34}$$

where $r_{\parallel}$ is the p-pol Fresnel complex amplitude reflection coefficient. Note that $r_{\perp,\parallel} = -1$ and 1 for a perfect electric conductor (i.e., a perfect reflector) and a perfect magnetic conductor, respectively.

Acknowledgments

This research was supported in part by an appointment to the Postgraduate Research Participation Program at the Air Force Institute of Technology administered by the Oak Ridge Institute for Science and Education through an interagency agreement between the U.S. Department of Energy and AFIT.

The views expressed in this paper are those of the authors and do not reflect the official policy or position of the U.S. Air Force, the Department of Defense, or the U.S. Government.

#182849 - $15.00 USD Received 4 Jan 2013; revised 18 Feb 2013; accepted 4 Mar 2013; published 12 Mar 2013